LA-UR- 09-01688

Title:

THE FLUID DYNAMIC APPROACH TO EQUIDISTRIBUTION METHODS FOR GRID GENERATION AND ADAPTATION

Author(s):

Gian Luca Delzanno 174843 - T-5/T-Division
John M Finn 113211 - T5/T-Division

Intended for:

SIAM Journal of Scientific Computing

The fluid dynamic approach to equidistribution methods for grid generation and adaptation

Gian Luca Delzanno [a], John M. Finn [a]

[a] *T-5, Applied Mathematics and Plasma Physics, Los Alamos National Laboratory, Los Alamos, NM 87545, USA*

Abstract

The equidistribution methods based on L_p Monge-Kantorovich optimization[Finn and Delzanno, submitted to SISC, 2009] and on the deformation [Moser, 1965; Dacorogna and Moser, 1990, Liao and Anderson, 1992] method are analyzed primarily in the context of grid generation. It is shown that the first class of methods can be obtained from a fluid dynamic formulation based on time-dependent equations for the mass density and the momentum density, arising from a variational principle. In this context, deformation methods arise from a fluid formulation by making a specific assumption on the time evolution of the density (but with some degree of freedom for the momentum density). In general, deformation methods do not arise from a variational principle. However, it is possible to prescribe an optimal deformation method, related to L_1 Monge-Kantorovich optimization, by making a further assumption on the momentum density. Some applications of the L_p fluid dynamic formulation to imaging are also explored.

Key words: Adaptive grid generation, Monge-Ampère equation, Monge-Kantorovich optimization, grid tangling, equidistribution, Newton-Krylov, multigrid preconditioning, moving meshes, image morphing
PACS: 02.70.-c

---

1 Introduction

Equidistribution is an established guiding principle in grid generation [1–4]. The idea is rather simple and therefore attractive: given a prescribed density or

---

Email addresses: `delzanno@lanl.gov` (Gian Luca Delzanno), `finn@lanl.gov` (John M. Finn).

monitor function ρ_1, one wants to generate a grid such that its cell volumes are inversely proportional to ρ_1. If ρ_1 represents the error in discretizing a PDE on a grid, equidistribution is even more attractive. The fact that equidistribution of the local truncation error leads to global minimization of the total error has recently been established [5,6].

Equidistribution alone cannot determine uniquely the new grid in two (2D) and three (3D) dimensions. Therefore the task becomes to determine a grid which is optimal in some sense among the infinite number of grids that satisfy a given equidistribution principle. There are several ways to do so. A common approach is to minimize a combination of grid property integrals (cost functions) with some global user-provided weights to determine the relative contributions of each term in the minimization procedure. For instance, a very popular approach is that of Brackbill and Saltzman [7], where a combination of integrals, smoothness (which measures global grid cell distortion), orthogonality, and cell volume (whose minimization gives equidistribution) has been employed. Notice that in this approach the *global* grid property integrals compete against each other and therefore the final grid never satisfies any constraint, including equidistribution. For this reason, we do not refer to these methods as equidistribution methods.

Another approach is to introduce a variational principle in which equidistribution is enforced *exactly* by a *local* Lagrange multiplier. (In this case, the Lagrange multiplier is computed as part of the minimization procedure and is not a global user-provided parameter.) This is the case of Refs. [8,9,?] where we introduced a powerful grid generation method based on L_2 Monge-Kantorovich (MK) optimization. [See also Ref. [10].] In short, the method minimizes the L_2 norm of the displacement of the grid points contrained to satisfy locally the equidistribution principle. This minimization procedure gives rise to the L_2 Monge-Ampère (MA) equation, a single, nonlinear equation with no tunable parameters, and with theorems of existence and uniqueness in 2D and 3D. In addition, the L_2 MA equation is elliptic and therefore one can use modern fast solvers for its solution. Indeed, in Ref. [8] we solved the L_2 MA equation by using Newton-Krylov methods with multigrid preconditioning and showed that L_2 MK optimization indeed provides a robust, efficient and scalable grid generation method. Recently, we have also extended L_2 MK optimization to L_p [11]. The L_p method shares many of the properties of L_2: it gives rise to a single, nonlinear, elliptic equation (of the form of a generalized MA equation) with no tunable parameters and for which theorems of existence and uniqueness exist. We have explored a number of values of p in the range $1 < p < 2.5$ and concluded that, at least for the example considered in Ref. [11], $p = 2$ gives the best quality grids according to several well-defined measures.

On the other hand, there is another grid generation method based on equidistribution in the literature. This is the deformation method proposed by Liao and Anderson [12], based on the general deformation procedure of Refs. [13,14]. To the best of our knowledge, is the only other method present in the literature that can achieve equidistribution exactly. As we shall discuss in some depth, there is no apparent connection between the deformation method and L_p MK optimization (or any other form of optimization) for general values of p. The deformation method is a ODE-based method where a continuous deformation of the initial grid by a suitable flow determines the new equidistributed grid. In principle the deformation method has considerable freedom associated with the choice of the flow. Analytical formulas for simple domains were given if in Refs. [12,15] but these choices can lead to bad quality grids (and even grid tangling), as shown in Ref. [8].

This paper complements and extends in several ways the work on some of the equidistribution methods used for grid generation (that is, the methods arising from L_p MK optimization as well as the deformation method). In particular

(1) We show that L_p MK optimization formulated in terms of the L_p MA equation is equivalent to a fluid dynamic formulation, based on time-dependent equations for the (mass) density and the momentum density.

(2) We show that the deformation method can be obtained from a fluid formulation by making a specific assumption on the time evolution of the density. With this assumption (but allowing a degree of freedom for the momentum density), any connection with the underlying variational principle of the L_p fluid dynamic formulation (and the related optimality) is lost.

(3) We show that it is possible to obtain an optimal deformation method by choosing a specific form of the momentum density as well as the mass density. With this choice, the optimal deformation method is then linked with L_1 MK optimization. However, there does not appear to be such a connection for $p \neq 1$.

(4) Toward the end of the paper, we explore the application of the L_p fluid dynamic formulation to find a warping transformation between two given images. We compare L_p with $1 < p < 2$ with L_2 and conclude that L_2 leads to a better warping algorithm, principally because of problems near the boundary for $p < 2$. However, we emphasize some limitations on the use of L_2 for this application.

This paper is organized as follows. In Sec. 2 we review briefly the minimization procedure behind L_p Monge-Kantorovich optimization. In Sec. 3 we discuss a time-dependent L_p variational principle which leads to the formulation of a set of fluid dynamics equations for the evolution of density and momentum. We show that these equations are equivalent to the L_p MK formulation. In Sec. 4 we review the deformation method, how it can be cast in a fluid framework and how it can be linked to the L_1 MK variational principle, using a specific choice of momentum density. In Sec. 5 we discuss implementation details. In

Sec. 6 we show numerical experiments with the fluid dynamics equations, check some of the theoretical predictions, and evaluate the results from the point of view of imaging applications. In Sec. 7 we draw conclusions. The Appendix deals with the proof that in the L_p fluid dynamic formulation the velocity is constant along streamlines.

2 L_p Monge-Kantorovich optimization

Let $X \subset \mathbb{R}^2$ be a bounded domain with boundary ∂X. We define a two-dimensional coordinate transformation in physical space between the coordinates of an initial grid $\mathbf{x}_0 = (x_0, y_0)$ and the ones of the final grid $\mathbf{x}_1 = (x_1, y_1)$ as $\psi : X \longrightarrow X$, i. e. $\mathbf{x}_1 = \psi(\mathbf{x}_0)$. We will assume that the boundary ∂X maps to itself. Both the initial grid $\mathbf{x}_0$ and the final grid $\mathbf{x}_1$ are mapped from the unit square $\boldsymbol{\xi} = (\xi, \eta) \in \Xi \equiv [0,1] \times [0,1]$, the logical space. The grid on Ξ is uniform.

Let us begin by reviewing the variational principle for L_p MK optimization [11], where we want to minimize:

$$F_p = \int_X \frac{|\mathbf{x}_1 - \mathbf{x}_0|^p}{p} \rho_0(\mathbf{x}_0) d\mathbf{x}_0 - \int_X \lambda(\mathbf{x}_1) \left[\rho_1(\mathbf{x}_1) J(\mathbf{x}_0) - \rho_0(\mathbf{x}_0)\right] d\mathbf{x}_0. \tag{1}$$

That is, we minimize the L_p norm of the distance $\mathbf{x}_1 - \mathbf{x}_0$ subject to the constraint that the Jacobian of the map satisfies a given equidistribution principle, that

$$J(\mathbf{x}_0) = \nabla \mathbf{x}_1(\mathbf{x}_0) = \frac{\partial x_1}{\partial x_0}\frac{\partial y_1}{\partial y_0} - \frac{\partial x_1}{\partial y_0}\frac{\partial y_1}{\partial x_0} \text{ equals } \frac{\rho_0(\mathbf{x}_0)}{\rho_1(\mathbf{x}_1)} \tag{2}$$

In Eq. (1), $\lambda(\mathbf{x}_1)$ is a Lagrange multiplier which enforces the equidistribution principle locally, and $\rho_0(\mathbf{x}_0)$ and $\rho_1(\mathbf{x}_1)$ are two given densities or monitor functions on X. The densities are positive and satisfy the normalization condition $\int_X \rho_0(\mathbf{x}_0) d\mathbf{x}_0 = \int_X \rho_1(\mathbf{x}_1) d\mathbf{x}_1 = 1$. Taking variations of F_p with respect to $\mathbf{x}_1$ we find [11]

$$\frac{\mathbf{x}_1 - \mathbf{x}_0}{|\mathbf{x}_1 - \mathbf{x}_0|^{2-p}} = -\nabla_1 \lambda(\mathbf{x}_0) \tag{3}$$

($\nabla_1 \equiv \nabla_{\mathbf{x}_1}$) or, alternatively,

$$\frac{\mathbf{x}_1 - \mathbf{x}_0}{|\mathbf{x}_1 - \mathbf{x}_0|^{2-p}} = \nabla \Phi(\mathbf{x}_0), \tag{4}$$

where $\nabla \equiv \nabla_{\mathbf{x}_0}$ and $\Phi(\mathbf{x}_0)$ is the L_p–Legendre transform of $\lambda(\mathbf{x}_1)$ [11]. Further manipulations lead to

$$\mathbf{x}_1 - \mathbf{x}_0 = a(\mathbf{x}_0)\nabla\Phi(\mathbf{x}_0) \tag{5}$$

with

$$a(\mathbf{x}_0) = |\nabla\Phi|^{\frac{2-p}{p-1}}. \tag{6}$$

Equation (5) is substituted into the equidistribution principle (2) to obtain the L_p MA equation [11]

$$\frac{\partial}{\partial x_0}\left(a(\mathbf{x}_0)\frac{\partial\Phi}{\partial x_0}\right) + \frac{\partial}{\partial y_0}\left(a(\mathbf{x}_0)\frac{\partial\Phi}{\partial y_0}\right) + \left[a(\mathbf{x}_0)\frac{\partial\Phi}{\partial x_0}, \, a(\mathbf{x}_0)\frac{\partial\Phi}{\partial y_0}\right] = \frac{\rho_0(\mathbf{x}_0)}{\rho_1(\mathbf{x}_1)} - 1. \tag{7}$$

The quantity $[f, g] = \epsilon_{ij}(\partial f/\partial x_{0,i})(\partial g/\partial x_{0,j})$ is the Poisson bracket (with summation over repeated indices), with $\epsilon_{12} = -\epsilon_{21} = 1$ and $\epsilon_{11} = \epsilon_{22} = 0$. The boundary conditions require mapping boundary points to boundary points. That is, for straight boundary segments we require

$$\hat{\mathbf{n}} \cdot \nabla\Phi = 0 \tag{8}$$

on the boundary ∂X, with $\hat{\mathbf{n}}$ the unit vector normal to the boundary. (Boundary conditions for curved boundary segments in $2D$ are described in Ref. [9].) Equation (7) is nonlinear and elliptic and has been solved [together with boundary conditions (8)] with Newton-Krylov techniques in Ref. [11].

3 Fluid dynamic formulation for L_p

Let us postulate a L_p variational principle to obtain a flow $\mathbf{x}(t)$ whose time-1 map $\mathbf{x}(0) \rightarrow \mathbf{x}(1)$ on the volume X is the optimal map $\mathbf{x}_0 \rightarrow \mathbf{x}_1$ of the L_p form of Monge-Kantorovich optimization [11]. This will allow us to determine the flow $\mathbf{x}(t)$ and the density $\rho(\mathbf{x}, t)$ which interpolates between $\rho_0(\mathbf{x}_0)$ and $\rho_1(\mathbf{x}_1)$ in an optimal manner. We begin by considering

$$W_p = \int_0^1 dt \int_X d\mathbf{x} \left\{ \frac{\rho(\mathbf{x},t)|\mathbf{v}(\mathbf{x},t)|^p}{p} + S(\mathbf{x},t)\left[\partial_t\rho(\mathbf{x},t) + \nabla\cdot(\rho(\mathbf{x},t)\mathbf{v}(\mathbf{x},t))\right]\right\}. \tag{9}$$

Minimization of the first term gives a 'most efficient' flow $\rho(\mathbf{x}, t)$ that transports from $\rho_0(\mathbf{x}_0)$ to $\rho_1(\mathbf{x}_1)$, i. e. satisfies $\rho(\mathbf{x}, 0) = \rho_0(\mathbf{x})$, $\rho(\mathbf{x}, 1) = \rho_1(\mathbf{x})$ on

X. The quantity $S(\mathbf{x},t)$ is a local Lagrange multiplier ensuring that $\rho(\mathbf{x},t)$ satisfies the continuity equation

$$\partial_t\rho + \nabla\cdot(\rho\mathbf{v}) = 0. \tag{10}$$

We will treat the $p = 2$ case and the case of more general p separately.

3.1 L_2 formulation

For the special case $p = 2$, Eq. (9) takes the form[16,17]

$$W_2 = \int_0^1 dt \int_X d\mathbf{x} \left\{ \frac{\rho(\mathbf{x},t)\mathbf{v}(\mathbf{x},t)^2}{2} + S(\mathbf{x},t)\left[\partial_t\rho(\mathbf{x},t) + \nabla\cdot(\rho(\mathbf{x},t)\mathbf{v}(\mathbf{x},t))\right] \right\}. \tag{11}$$

In a fluid dynamics context, the first term in the integrand represents the kinetic energy density. Taking the first variation with respect to $\rho(\mathbf{x},t)$ and $\mathbf{v}(x,t)$, respectively, we find, upon integrating by parts in $\mathbf{x}$ and t

$$\mathbf{v} = \nabla S, \tag{12}$$

$$\partial_t S + \mathbf{v}\cdot\nabla S = \frac{\mathbf{v}^2}{2}. \tag{13}$$

(The endpoint terms obtained from integrating by parts in time are zero because ρ is specified there. The terms on ∂X are zero because the normal component $\mathbf{v}\cdot\hat{\mathbf{n}}$ equals zero there.) Substituting, we obtain

$$\partial_t S = -\frac{1}{2}|\nabla S|^2. \tag{14}$$

This is the Hamilton-Jacobi or ray optics (Eikonal) equation. We use this equation together with the continuity equation (with Eq. (12))

$$\partial_t\rho + \nabla\cdot(\rho\nabla S) = 0 \tag{15}$$

in the following manner: we choose an initial condition $S(\mathbf{x},0)$ and fix the initial density $\rho(\mathbf{x},0) = \rho_0(\mathbf{x})$. We then integrate Eqs. (14), (15) in time to $t = 1$, and consider the residual $R(\mathbf{x}) \equiv \rho(\mathbf{x},1) - \rho_1(\mathbf{x})$. We vary $S(\mathbf{x},0)$ to drive the residual R to zero on V. In practice this is achieved by Newton's method, discussed in Sec. 5.

One more observation is in order. If take the gradient of Eq. (14) and use Eq. (12), we find

$$\partial_t \mathbf{v} = -\frac{1}{2}\nabla \mathbf{v}^2.$$

Since $\nabla \times \mathbf{v} = 0$, we conclude

$$\partial_t \mathbf{v} + \mathbf{v} \cdot \nabla \mathbf{v} = 0. \tag{16}$$

That is, Eqs. (10) and (16) are the equations for a pressureless irrotational fluid. (See Ref. [18].) This last relation implies that $\mathbf{v}(\mathbf{x}, t)$ is constant along the trajectory, i. e.

$$\mathbf{v}(\mathbf{x}, t) = \mathbf{v}(\mathbf{x}_0(\mathbf{x}, t), 0) = \mathbf{v}_0(\mathbf{x}_0), \tag{17}$$

where $\mathbf{x}_0(\mathbf{x}, t)$ is the initial position of the fluid element located at $\mathbf{x}$ at time t. This means that the orbit $d\mathbf{x}/dt = \mathbf{v}(\mathbf{x}, t)$ is a straight line given by

$$\mathbf{x}(t) = \mathbf{x}_0 + t\mathbf{v}_0(\mathbf{x}_0). \tag{18}$$

Its time-1 map $\mathbf{x}_0 \to \mathbf{x}_1 = \mathbf{x}(1)$ is given by

$$\mathbf{x}(1) = \mathbf{x}_0 + \mathbf{v}(\mathbf{x}_0) = \mathbf{x}_0 + \nabla S(\mathbf{x}_0, 0) = \nabla \left[\frac{\mathbf{x}_0^2}{2} + S(\mathbf{x}_0, 0)\right]. \tag{19}$$

In general the time-1 map for a gradient flow is not a gradient map. However, in this special case with constant velocity trajectories, this property does hold.

It is easy to see now that this flow produces the same map as the usual L_2 Monge-Kantorovich theory, i. e. by solving the Monge-Ampère equation [8]. Indeed, the flow in Eq. (19) takes $\rho_0(\mathbf{x}_0)$ to $\rho_1(\mathbf{x}_1)$ and is a gradient map. Thus, $S(\mathbf{x}_0, 0)$ is a solution of the Monge-Ampère equation, and these solutions are known to be unique.

3.2 L_p formulation

Taking variations of W_p of Eq. (9) with respect to $\rho(\mathbf{x}, t)$ and $\mathbf{v}(x, t)$ leads to

$$\mathbf{v} = |\mathbf{v}|^{2-p}\nabla S, \tag{20}$$

$$\partial_t S + \mathbf{v} \cdot \nabla S = \frac{|\mathbf{v}|^p}{p}, \tag{21}$$

with the integrations by parts in t and $\mathbf{x}$ justified as in Sec. 2.1, assuming the normal component $\mathbf{v}\cdot\hat{\mathbf{n}}$ vanishes on the boundary ∂X. Substituting, and defining q such that $1/p + 1/q = 1$, we find

$$|\mathbf{v}| = |\nabla S|^{\frac{1}{p-1}} = |\nabla S|^{q-1} \quad \text{and} \quad \mathbf{v} = |\nabla S|^{\frac{2-p}{p-1}}\nabla S = |\nabla S|^{q-2}\nabla S, \tag{22}$$

$$\partial_t S = -\frac{p-1}{p}|\nabla S|^{\frac{p}{p-1}} = -\frac{1}{q}|\nabla S|^{q}. \tag{23}$$

We solve this L_p analog of the Hamilton-Jacobi equation coupled with the continuity equation (10) with $\mathbf{v} = |\nabla S|^{q-2}\nabla S$. As for L_2, we drive the residual $R(\mathbf{x}) \equiv \rho(\mathbf{x},1) - \rho_1(\mathbf{x})$ to zero using Newton's method, by varying $S(\mathbf{x},0)$.

We now show that Eq. (16) holds for L_p as it does for L_2. The outline of the derivation is the following: we differentiate Eq. (12) with respect to time to obtain

$$\partial_t \mathbf{v} = -f^{\frac{3-p}{p-1}}\left[\nabla f + \frac{2-p}{p-1}\hat{\mathbf{e}}\hat{\mathbf{e}}\cdot\nabla f\right], \tag{24}$$

where $f = |\nabla S|$ and $\hat{\mathbf{e}} = \nabla S/|\nabla S|$. From Eq. (12) we conclude

$$\nabla\times\mathbf{v} = \frac{2-p}{p-1}f^{\frac{3-2p}{p-1}}\nabla f\times\nabla S; \tag{25}$$

this implies

$$\begin{gathered}\partial_t\mathbf{v} - \mathbf{v}\times\nabla\times\mathbf{v} + \nabla\frac{\mathbf{v}^2}{2} = 0 \quad \text{or} \\ \partial_t\mathbf{v} + \mathbf{v}\cdot\nabla\mathbf{v} = 0.\end{gathered} \tag{26}$$

For more details see Appendix A.

As in Sec. 2.1, this implies that the orbits $\mathbf{x}(t)$ are constant velocity straight lines, i. e. Eqs. (17) and (18) again hold. However, Eq. (19) is replaced by

$$\mathbf{x}(1) = \mathbf{x}_0 + \mathbf{v}(\mathbf{x}_0) = \mathbf{x}_0 + |\nabla S(\mathbf{x}_0,0)|^{\frac{2-p}{p-1}}\nabla S(\mathbf{x}_0,0). \tag{27}$$

This map $\mathbf{x}_0 \to \mathbf{x}_1 = \mathbf{x}(t=1)$ is not a gradient map. However, this equation is of the same form as Eqs. (5), (6) (Eq. (14) of Ref. [11]) which, when substituted into the continuity equation, leads to the L_p Monge-Ampère (L_p MA) equation 7. It was shown in Ref. [11] that the L_p MA equation is a generalized Monge-Ampère equation and is elliptic. Further, the boundary condition $\mathbf{v}\cdot\hat{\mathbf{n}} =$

$\hat{\mathbf{n}} \cdot \nabla S = 0$ on ∂X is identical to that used in Ref. [11]. We conclude that the time-1 map from the L_p flow produces the identical map as the L_p map found in Ref. [11]. This conclusion is based on the known uniqueness properties of the L_p MA equation, which is a generalized Monge-Ampère equation.

3.3 Smoothed L_1

For a smoothed L_1 variational principle such as the one introduced in Ref. [11], we use the variational

$$W_1(\varepsilon) = \int_0^1 dt \int_X d\mathbf{x} \left\{ \rho(\mathbf{x},t) \left[\sqrt{\varepsilon^2 + \mathbf{v}(\mathbf{x},t)^2} - \varepsilon \right] + S(\mathbf{x},t) \left[\partial_t \rho(\mathbf{x},t) + \nabla \cdot (\rho(\mathbf{x},t)\mathbf{v}(\mathbf{x},t)) \right] \right\} . \quad (28)$$

Taking variations with respect to $\rho(\mathbf{x},t)$ and $\mathbf{v}(\mathbf{x},t)$ we obtain, similar to the results of Sec. 3.2,

$$\begin{aligned} \mathbf{v} &= \frac{\varepsilon \nabla S}{\sqrt{1 - |\nabla S|^2}} \\ \partial_t S &= \left[\varepsilon \sqrt{1 - |\nabla S|^2} - \varepsilon \right] . \end{aligned} \quad (29)$$

Similar manipulations to those in Appendix A show that

$$\partial_t \mathbf{v} + \mathbf{v} \cdot \nabla \mathbf{v} = 0.$$

Again, the velocity is constant along the streamlines, $\mathbf{v}(\mathbf{x},t) = \mathbf{v}_0(\mathbf{x}_0)$. Further, the time-1 map

$$\mathbf{x}(t=1) = \mathbf{x}_0 + \frac{\varepsilon \nabla S}{\sqrt{1 - |\nabla S|^2}} \quad (30)$$

is identical to the smoothed L_1 map of Ref. [11], Eq. (39).

4 Optimality and the deformation method

There is one other equidistribution method in the literature, the deformation method of Liao and Anderson [12]. It is based on the method of Moser [13], Banyaga [19] and Dacorogna and Moser [14]. Originally the method was designed to handle only a density $\rho_0(\mathbf{x}_0) \neq 1$ with $\rho_1(\mathbf{x}_1) = 1$ but it was modified in Ref. [15] to treat $\rho_1(\mathbf{x}_1) \neq 1$ with $\rho_0(\mathbf{x}_0) = 1$. The deformation method was applied to 2D grid generation in Refs. [20,21] and to moving meshes in Refs. [22,23]. Other applications of the deformation method can be found in Refs. [24,25].

Let us now review this method, which is based on the solution of a second order time-dependent ODE (in 2D) and reaches the new equidistributed grid by a continuous deformation of the initial grid. Specifically, the method consists of two steps. Here we treat the general case of $\rho_0(\mathbf{x}_0) \neq 1$ and $\rho_1(\mathbf{x}_1) \neq 1$, which can be found in Ref. [25]. First, one needs to find a solution of

$$\begin{aligned} &\nabla \cdot \mathbf{u}(\mathbf{x}) = \rho_0(\mathbf{x}) - \rho_1(\mathbf{x}) \equiv g(\mathbf{x}) \\ &\mathbf{u} \cdot \hat{\mathbf{n}} = 0 \quad \text{on } \partial X. \end{aligned} \tag{31}$$

It is obvious that Eq. (31) does not have a unique solution. Then, the following system of equations needs to be solved for $\mathbf{x}(\mathbf{x}_0, t)$ with $t \in [0, 1]$

$$\begin{aligned} &\frac{d\mathbf{x}}{dt} = \mathbf{v}(\mathbf{x}, t) = \frac{\mathbf{u}(\mathbf{x})}{t\rho_1(\mathbf{x}) + (1-t)\rho_0(\mathbf{x})} \\ &\mathbf{x}(\mathbf{x}_0, t = 0) = \mathbf{x}_0 \end{aligned} \tag{32}$$

and the new grid is obtained as

$$\mathbf{x}(t = 1) = \mathbf{x}_0. \tag{33}$$

The derivation [12,15,25] proceeds as follows: define the function

$$H(\mathbf{x}, t) = [t\rho_1(\mathbf{x}) + (1-t)\rho_0(\mathbf{x})] \det\nabla\mathbf{x}(\mathbf{x}_0, t). \tag{34}$$

The next step is to show that H does not depend on time along the trajectory, i. e. $dH/dt = \partial H/\partial t + \mathbf{v}(\mathbf{x}, t) \cdot \nabla H = 0$. Thus, $H(\mathbf{x}_0, 0) = H(\mathbf{x}_1, 1)$ implies

$$\rho_0(\mathbf{x}_0) = \rho_1(\mathbf{x}_1)\det\nabla\mathbf{x}_1 = \rho_1(\mathbf{x}_1)J(\mathbf{x}_0), \tag{35}$$

showing that the equidistribution principle is satisfied.

In order to compute a grid by this method, Liao and Anderson [12], and Liao and Su [15] have proposed analytical solutions valid for simple domains such as the unit square. One example of these solutions is

$$v_x(x,y) = \frac{1}{2}\left[\int\limits_0^x g(t,y)dt - h(x)\int\limits_0^1 g(t,y)dt + h'(y)\int\limits_0^x\int\limits_0^1 g(s,t)dtds\right], \tag{36}$$

$$v_y(x,y) = \frac{1}{2}\left[\int\limits_0^y g(x,t)dt - h(y)\int\limits_0^1 g(x,t)dt + h'(x)\int\limits_0^y\int\limits_0^1 g(t,s)dtds\right], \tag{37}$$

where $h \in C^1$ is any function on $[0,1]$ such that

$$h(0) = h'(0) = h'(1) = 0, \quad h(1) = 1. \tag{38}$$

However, these solutions are notan optimal choice in any sense. Indeed, in Ref. [8] we showed for a challenging example, with $\rho_1 = 1$ and $\rho_1(\mathbf{x}_1)$ fairly complex, the deformation method [with the velocity field described by Eqs. (36) and (37) with $h(x) = [1 + \cos(\pi(x-1))]/2]$ produced highly elongated cells which resulted in grid tangling for a 64 × 64 grid. In a later paper, Liu et al. [21] used $\mathbf{u}(\mathbf{x}) = \nabla w(\mathbf{x})$, leading to

$$\begin{aligned} &\nabla^2 w = \rho_0(\mathbf{x}) - \rho_1(\mathbf{x}) \ \text{ on } X, \\ &\nabla w \cdot \hat{\mathbf{n}} = 0 \ \text{ on } \partial X. \end{aligned} \tag{39}$$

This obviously has a unique solution for $\mathbf{u}$. This gradient flow approach is also the choice adopted in Ref. [25].

It is clear that in the deformation method there is freedom in choosing the velocity field. The remainder of this section will be devoted to understand how this flow can be chosen such that the deformation method can be linked to a variational principle.

First, we show that the deformation method can be expressed in fluid terms similar to that in Section 3, in order to make the derivation in Eqs. (31)-(35) more transparent. Suppose we assume that the density evolves in time according to

$$\rho(\mathbf{x},t) = \rho_1(\mathbf{x})t + (1-t)\rho_0(\mathbf{x}), \tag{40}$$

a linear interpolation in time of the initial and final densities. Since $\partial\rho/\partial t = \rho_1 - \rho_0$, substitution into the continuity equation (10) leads to the following equation for the momentum density $\mathbf{u}(\mathbf{x}) = \rho(\mathbf{x},t)\mathbf{v}(\mathbf{x},t)$:

$$\nabla \cdot \mathbf{u}(\mathbf{x}) = \rho_0(\mathbf{x}) - \rho_1(\mathbf{x}). \tag{41}$$

Furthermore, the equation for the flow can now be cast in the form

$$\frac{d\mathbf{x}}{dt} = \mathbf{v}(\mathbf{x}, t) = \frac{\mathbf{u}(\mathbf{x})}{\rho(\mathbf{x}, t)} = \frac{\mathbf{u}(\mathbf{x})}{\rho_1(\mathbf{x})t + (1-t)\rho_0(\mathbf{x})}. \tag{42}$$

Now the link between the fluid dynamic L_p formulation and the deformation method becomes clear. In the fluid dynamic L_p formulation, we solve the continuity equation (10) and Eqs. (22) and (23) for the time-dependent velocity field. The continuity equation transports the density from ρ_0 to ρ_1 according to this optimal flow. The latter is obtained such to minimize the first term in Eq. (9) and is dependent on p. As soon as we make a specific assumption on the time evolution of the density such as Eq. (40), the continuity equation leads to an equation for the velocity field consistent with this assumption. Clearly this velocity field will not be optimal [since the optimal one is determined by Eqs. (22) and (23)] and therefore any relationship with the underlying L_p variational principle is lost. Thus, it appears that the deformation method can be formulated in a fluid context at the price of losing the connection with a variational principle and its associated optimality.

One further comment is in order. One could in principle consider more complex time dependencies of the density than that in Eq. (40). For instance, one could consider

$$\rho(\mathbf{x}, t) = \rho_1(\mathbf{x})t + (1-t)\rho_0(\mathbf{x}) + t(1-t)\rho_2(\mathbf{x}), \tag{43}$$

with ρ_2 any function on X. Notice that the density ρ at $t = 0$ and $t = 1$ are unchanged by this term. Substitution of Eq. (43) into the continuity equation (10) as before leads to

$$\nabla \cdot \mathbf{u}(\mathbf{x}, t) = \rho_0(\mathbf{x}) - \rho_1(\mathbf{x}) + (2t-1)\rho_2(\mathbf{x}). \tag{44}$$

Writing $\rho\mathbf{v} = \mathbf{u}(\mathbf{x}, t) = \mathbf{u}_1(\mathbf{x}) + t\mathbf{u}_2(\mathbf{x})$, we find

$$\begin{aligned} \nabla \cdot \mathbf{u}_1(\mathbf{x}) &= \rho_0(\mathbf{x}) - \rho_1(\mathbf{x}) - \rho_2(\mathbf{x}), \\ \nabla \cdot \mathbf{u}_2(\mathbf{x}) &= 2\rho_2(\mathbf{x}). \end{aligned} \tag{45}$$

Furthermore, the solution of

$$\frac{d\mathbf{x}}{dt} = \mathbf{v} = \frac{\mathbf{u}_1(\mathbf{x}) + \mathbf{u}_2(\mathbf{x})t}{\rho_1(\mathbf{x})t + (1-t)\rho_0(\mathbf{x}) + t(1-t)\rho_2(\mathbf{x})} \tag{46}$$

leads to $\rho(\mathbf{x}, 0) = \rho_0(\mathbf{x})$ and $\rho(\mathbf{x}, 1) = \rho_1(\mathbf{x})$. That is, Eqs. (45) and (46) represent an alternative deformation method which still satisfies the same equidistribution principle. (Notice as before that Eqs. (45) and (46) do not have unique solutions.) Of course, one could generalize the deformation method even further by expanding the density in a series of the form $\sum_{m,n} t^m(1-t)^n \rho_{m,n}(\mathbf{x})$, resulting in a more complex method involving a more general momentum density $\mathbf{u}(\mathbf{x},t) = \sum_k t^k \mathbf{u}_k(\mathbf{x})$. This little exercise reveals that there is nothing special behind the assumption (40) leading to the deformation method. However, it is not at all clear that the added complexity in, for example, Eq. (43), leads to much.

The considerations above point clearly to the importance of the choice of the flow in determining the new equidistributed grid for the deformation method. The question then becomes whether it is possible to pick this flow in such a way to regain a connection with a variational principle or, in other words, to obtain an optimal deformation method. It turns out that the answer to this question has been provided by Evans and Gangbo [26]. This was done (see also Trudinger and Wang [27] and Caffarelli *et al.* [28]) in the context of finding an alternative proof of the existence of a solution for the L_1 MK optimization problem (and not in the context of grid generation.) The proof in Ref. [26] is quite complex and we refer the interested reader there for mathematical details. Here we only report the results. Ref. [26] starts with solutions of the equation

$$\nabla \cdot \mathbf{u}(\mathbf{x}) = \rho_0(\mathbf{x}) - \rho_1(\mathbf{x}) \quad \text{with} \quad \mathbf{u}(\mathbf{x}) = |\nabla W(\mathbf{x})|^{q-2}\nabla W(\mathbf{x}) = b(\mathbf{x})\nabla W. \tag{47}$$

(As noted earlier, $q-2$ equals $= (2-p)/(p-1)$.) We require $\hat{\mathbf{n}} \cdot \nabla W = 0$ on ∂X. There is some similarity with Eq. (22), but note that here the momentum density $\rho\mathbf{v} = \mathbf{u}(\mathbf{x})$ is of the form in Eq. (47), whereas in Eq. (22) the *velocity* $\mathbf{v} = \mathbf{u}/\rho$ is of this form. The next step is to solve $d\mathbf{x}/dt = \mathbf{v} = \mathbf{u}/\rho$, where $\rho(\mathbf{x},t)$ is of the form (40), i. e.

$$\begin{aligned} \frac{d\mathbf{x}}{dt} &= \frac{|\nabla W(\mathbf{x})|^{q-2}\nabla W(\mathbf{x})}{t\rho_1(\mathbf{x}) + (1-t)\rho_0(\mathbf{x})} \\ \mathbf{x}(0) &= \mathbf{x}_0. \end{aligned} \tag{48}$$

Evans and Gangbo [26] proved that the time-1 map produced by this method $\mathbf{x}_1 = \mathbf{x}(\mathbf{x}_0, 1)$ is, in the limit $p \to 1$, the solution of the L_1 MK optimization problem [Eq. (1) with $p = 1$].

Thus, when $p \to 1$ Eqs. (47) and (48) give the *optimal deformation method,* which is linked to the L_1 variational principle. We must emphasize that, although the flow discussed here and the flow of Sec. 3.2 in the limit $p \to 1$ produce the same optimal L_1 map, the flows are not identical and the densities are also distinct. As we discuss further in Sec. 6, the density found using the methods of Sec. 3.2 is *not* of the form (40). Related to this is the fact that the momentum density in Eq. (47) depends on $\mathbf{x}$ but not on time, whereas

$\mathbf{u} = \rho\mathbf{v}$ of Sec. 3.2 has explicit time dependence.

A few considerations are in order. First, note that Eq. (39) is the special case of Eq. (47), with $p = 2$. Note also that, unlike Eq. (39), Eq. (47) is nonlinear and therefore solution for W requires more sophisticated numerical techniques such as the Newton-Krylov method [29]. Another point relates to the similarity of Eq. (47) with Eq. (22), as noted in the previous paragraph.

Notice the similarities and differences between Eq. (47) and Eq. (7), the L_p MA equation. The first two terms of Eq. (7) correspond to the left hand side of Eq. (47). However, Eq. (47) does not contain the nonlinearities associated with the Poisson bracket in Eq. (7). Also, in Eq. (47) we have $\rho_1(\mathbf{x}_0)$ while in Eq. (7) we have $\rho_1(\mathbf{x}_1)$, which introduces an additional source of nonlinearity.

Finally, we comment that Ref. [11] shows that a grid generation method based on L_p MK optimization with $p \longrightarrow 1$ is more prone to generate highly distorted grid cells near the boundary. This observation leads to the conclusion that the optimal distortion method (with $p = 1$) might not be suitable for grid generation applications.

It appears that this connection between the deformation method of grid generation and L_1 Monge-Kantorovich optimization has not been reported in the literature, nor have the boundary problems of L_p with $p \longrightarrow 1$.

5 Numerical implementation

In this section we discuss the details of the numerical implementation for the fluid dynamic formulation characterized by Eqs. (10), (22) and (23), and for the optimal deformation method, Eqs. (47) and (48).

In the following, wherever needed, we use a standard, non-linear Newton-Krylov solver [29], where we set the absolute error tolerance $\tau_a = 10^{-4}$ and the relative error tolerance $\tau_r = 10^{-4}$. The inner iterations are performed using the GMRES scheme, without restarting. The forcing parameter η_k is constant $\eta_k = 10^{-3}$. Since we do not focus on performance issues in this paper, we do not use a preconditioner for the GMRES iterations.

5.1 *Fluid Dynamic formulation*

We use a uniform grid in x_0, y_0 even when $\rho_0 \neq 1$?, although this choice may be suboptimal. To discretize Eqs. (10), (22) and (23), we consider a uniform grid in $\mathbf{x}$, with grid spacing Δx and Δy in the x and y directions, respectively.

The unknowns $S_{i,j}$ are located at cell centers (i and j label cell centers in the x and y directions) and we use ghost cells to enforce boundary conditions on S. Moreover, the velocity field $\mathbf{v}_{i+1/2,j+1/2}$ is located at vertices while the density $\rho_{i,j}$ is located at cell centers. The first order derivatives of S are computed as

$$\left(\frac{\partial S}{\partial x}\right)_{i+1/2,j+1/2} \approx \frac{S_{i+1,j}+S_{i+1,j+1}-S_{i,j}-S_{i,j+1}}{2\Delta x}, \tag{49}$$

$$\left(\frac{\partial S}{\partial y}\right)_{i+1/2,j+1/2} \approx \frac{S_{i,j+1}+S_{i+1,j+1}-S_{i,j}-S_{i+1,j}}{2\Delta y}. \tag{50}$$

We will also need ∇S at cell centers:

$$(\nabla S)_{i,j} = \frac{(\nabla S)_{i+1/2,j+1/2}+\nabla S|_{i+1/2,j-1/2}+\nabla S|_{i-1/2,j+1/2}+\nabla S|_{i-1/2,j-1/2}}{4}. \tag{51}$$

Consequently

$$\mathbf{v}_{i+1/2,j+1/2} = |\nabla S|^{q-2}_{i+1/2,j+1/2}(\nabla S)_{i+1/2,j+1/2}. \tag{52}$$

The discretization at cell centers of the term $\nabla\cdot(\rho\mathbf{v})$ in Eq. (10) is performed in a similar manner as in Eqs. (49) and (50) (interchanging $i+1/2 \longrightarrow i$ and $j+1/2 \longrightarrow j$). In this case, the density $\rho_{i+1/2,j+1/2}$ in the vertices is needed and this is obtained from second order extrapolation from the values $\rho_{i,j}$ at cell centers. Finally, we have

$$\frac{\partial S_{i,j}}{\partial t} = -\frac{p-1}{p}|\nabla S|^{\frac{p}{p-1}}_{i,j} \tag{53}$$

$$\frac{\partial \rho_{i,j}}{\partial t} = -\nabla\cdot(\rho\mathbf{v})_{i,j} \tag{54}$$

for $t \in (0,1)$. The ODEs (53) and (54) are solved with a second order Runge-Kutta scheme. We have performed convergence studies changing time step Δt of the Runge-Kutta solver and grid spacings Δx and Δy (not shown) and choose $\Delta t = 0.01$ for the results presented in this paper.

The boundary conditions for S are implemented via ghost cells [8]. If we consider for instance the $x = 1$ segment of ∂X, where $\partial S/\partial x = 0$, we have $S_{n_x+1,j} = S_{n_x,j}$, second order accurate because this segment of the boundary is at $x_{n_x+1/2} = 1$. (We use a similar formulation for the other boundary segments). For the corner ghost cells, we impose

$$S_{n_x+1,n_y+1} = S_{n_x+1,n_y} = S_{n_x,n_y+1} = S_{n_x,n_y}$$

at the top-right corner and similarly for the other corners. Here n_x and n_y label the number of grid cells in the x and y directions.

As discussed in Sec. 3, the fluid dynamic formulation proceeds as follows: instead of specifying $\rho(\mathbf{x},0)$ and $S(\mathbf{x},0)$ as initial conditions, we have $\rho(\mathbf{x},0) = \rho_0(\mathbf{x})$ and $\rho(\mathbf{x},1) = \rho_1(\mathbf{x})$. Therefore one needs to start the integration of Eqs. (53) and (54) with an initial guess for $S(\mathbf{x},0)$; we then iterate until $\rho(\mathbf{x},1) = \rho_1$ within a given tolerance. This is done by Newton-Krylov methods, where we drive to zero the residual $R = \rho(\mathbf{x},t=1) - \rho_1(\mathbf{x})$.

5.2 Optimal deformation method

As discussed in Ref. [8], it is efficient to solve equations like Eq. (47) for W on a reference grid and then, as $\mathbf{x}$ is updated in time according to Eqs. (48), use a cubic spline interpolation to obtain the velocity field at the new $\mathbf{x}$ positions. In order to solve Eq. (47), we use a uniform reference grid with grid spacing Δx and Δy where the unknowns are located at cell centers $W_{i,j}$ and the boundary conditions are imposed via ghost cells. This is the same as what is done in Sec. 5.1 and we omit further details here.

The discretization of the right hand side of Eq. (47) is done with a 5-point stencil:

$$\nabla\cdot(\nabla W)\,|_{i,j} \approx b_{i+1/2,j}\frac{W_{i+1,j}}{\Delta x^2} - \left(b_{i+1/2,j} + b_{i-1/2,j}\right)\frac{W_{i,j}}{\Delta x^2} + b_{i-1/2,j}\frac{W_{i-1,j}}{\Delta x^2} + \\ b_{i,j+1/2}\frac{W_{i,j+1}}{\Delta y^2} - \left(b_{i,j+1/2} + b_{i,j-1/2}\right)\frac{W_{i,j}}{\Delta y^2} + b_{i,j-1/2}\frac{W_{i,j-1}}{\Delta y^2} \tag{55}$$

where

$$b_{i+1/2,j+1/2} \approx \left[\left(\frac{W_{i+1,j+1} + W_{i+1,j} - W_{i,j-1} - W_{i,j}}{2\Delta x}\right)^2 + \left(\frac{W_{i+1,j+1} - W_{i+1,j} + W_{i,j-1} - W_{i,j}}{2\Delta y}\right)^2\right]$$

and the off-vertex values $b_{i+1/2,j}$ are averaged:

$$b_{i+1/2,j} = \frac{b_{i+1/2,j+1/2} + b_{i+1/2,j-1/2}}{2} \tag{57}$$

(and similarly for $b_{i,j+1/2}$).

The solution of Eq. (47) is obtained by Newton-Krylov methods, while the integration of Eqs. (48) is obtained by the second order Runge-Kutta method (again with time step $\Delta t = 0.01$).

6 Results

In this section, we investigate solutions of the L_p equations. We first check some of the theoretical predictions of Secs. 3 and 4. That is, we compare the grids obtained by solving the generalized MA equation (7) and the L_p fluid dynamic formulation described in Eqs. (10), (22) and (23). We then show studies of the time evolution of the density in the fluid dynamic formulation. We also compare the fluid dynamic formulation with the optimal deformation method (in the limit $p \longrightarrow 1$). Finally, we discuss some aspects of the fluid dynamic formulation applied to imaging.

6.1 Comparison of the fluid dynamic formulation with the L_p MK method

In this subsection, we compare the grid obtained by the fluid dynamic formulation (Sec. 3) with the L_p MK method, where the generalized MA equation (7) is solved to get the final map (Sec. 2). We choose the following example

$$\begin{aligned}\rho_0(\mathbf{x}_0) &= \frac{C_1}{1+4\left[(x_0-0.7)^2+(y_0-0.8)^2\right]}\\ \rho_1(\mathbf{x}_1) &= \frac{C_2}{1+64\left[(x_1-0.2)^2+(y_1-0.3)^2\right]}\end{aligned} \tag{58}$$

where C_1 and C_2 are normalization constants such that $\int_X \rho_0(\mathbf{x}_0)d\mathbf{x}_0 = \int_X \rho_1(\mathbf{x}_1)d\mathbf{x}_1 = 1$. The density ρ_0 is fairly broad: the ratio of the maximum to the minimum density ρ_{max}/ρ_{min} is 5.5. This ratio for ρ_1 is much larger, about 73. Thus, this example is rather challenging. The corresponding 16×16 grids are shown in Fig. 1, for $p = 2, 1.25, 1.1, 1.01$. The solid line corresponds to the grid obtained with the fluid dynamic formulation while the dashed line corresponds to the L_p MK method. This figure shows that the two methods produce approximately the same grids (consistent with truncation errors), with larger differences as $p \longrightarrow 1$. These differences decrease when the resolution is increased (not shown). As discussed in Ref. [11], it is apparent that, as $p \longrightarrow 1$, the grid cells are much more stretched relative to the $p = 2$ case and there is a crease connecting the upper-right corner with the peak of ρ_1 at $x_1 = 0.2$, $y_1 = 0.3$. This is associated with the behavior near the boundary and is related to the fact that domains with fixed boundary points (such as the corners in the unit square) violate the Eikonal equation [11]. For this reason, in Ref. [11] we concluded that L_p for $p \longrightarrow 1$ is not suitable for grid generation applications in such domains.

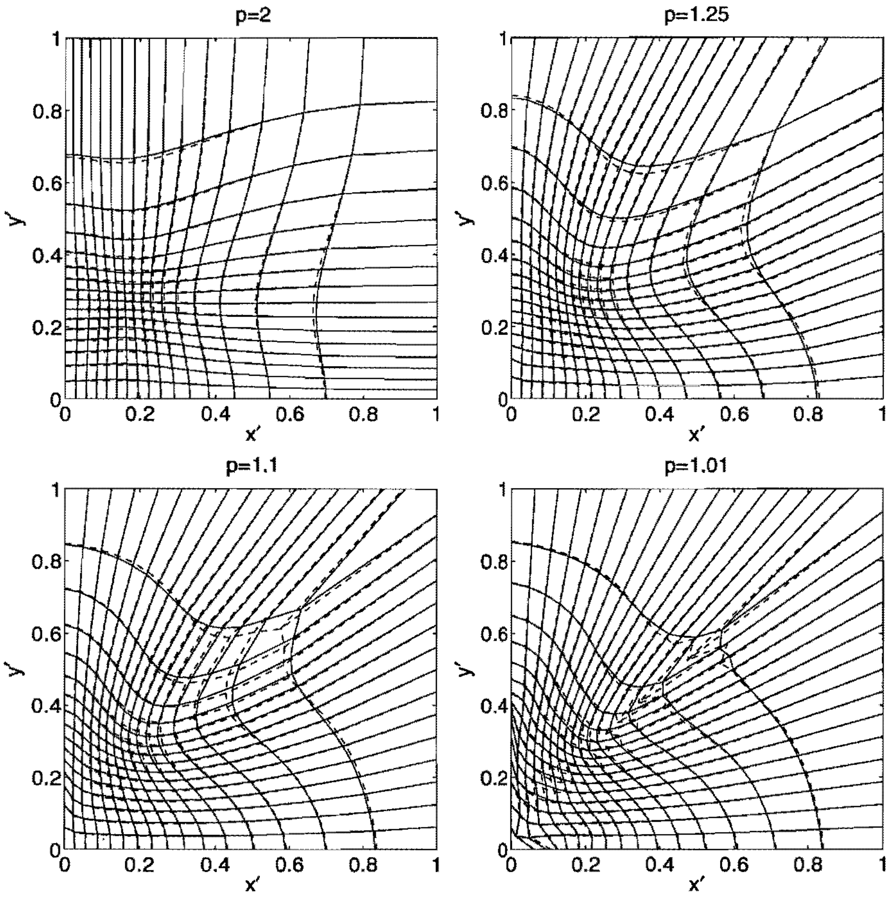

Fig. 1. Grid lines, i. e. contours $x(x', y') = \text{const}$ and $y(x', y') = \text{const}$ for the fluid dynamic formulation (solid line) and the L_p MK method (dashed line) with $p = 2, 1.25, 1.10, 1.01$ (16×16 cells).

6.2 Time evolution of the density for the fluid dynamic formulation

In this subsection, we discuss the time evolution of the density obtained by the fluid dynamic formulations of Secs. 3 and 4. This is important in light of the results of Sec. 4, where we showed that the deformation method (optimal or not) can be obtained from a fluid dynamic formulation by assuming the form of the density in Eq. (40). Here we check whether this interpolated density is related to the density obtained by the L_p fluid dynamic formulation of Secs. 3.1, 3.2.

We focus on the example with densities given by Eq. (58). The results for $p = 2$ are shown in Fig. 2, which shows 11 snapshots (equally spaced in time) of the density evolution. Each snapshot consists of 15 equally spaced contours of the density, between the minima and maximum at each time. It is evident in Fig. 2 that the peak of the density (starting at $x = 0.7$, $y = 0.8$) is advected

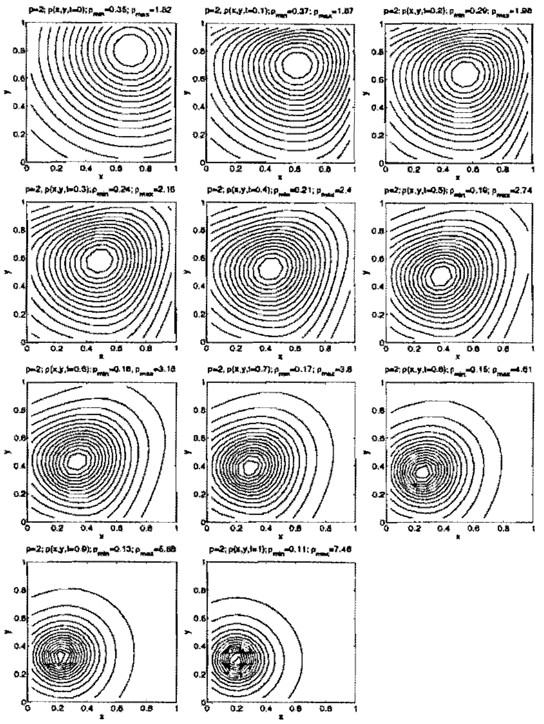

Fig. 2. Contours of the density evolution from the fluid dynamic formulation with $p = 2$ for the densities given by Eqs. (58). Each subplot shows 15 equally spaced density contours with the maximum and minimum contours indicated.

toward its final position ($x = 0.2$, $y = 0.3$). Around the peak the contours remain roughly circular, although there is some distortion near the boundary.

Figure 3 shows the evolution of the density for $p = 1.01$. The evolution is similar to that of Fig. 2, although there is a much stronger interaction with the boundary (particularly at early times, near the upper-right corner). The crease (discussed in the context of Fig. 1) connecting the upper-right corner with the peak of the density is also visible in the contours. Although there are some differences between the density evolution for $0 < t < 1$, these two are quite different from the linear interpolation of the density between ρ_0 and ρ_1 plotted in Fig. 4. This figure shows clearly how the linearly interpolated density exhibits structures associated with the two peaks of ρ_0 and ρ_1. Rather, the densities in Figs. 2 and 3 show simple motion of the maxima between those of ρ_0 and ρ_1.

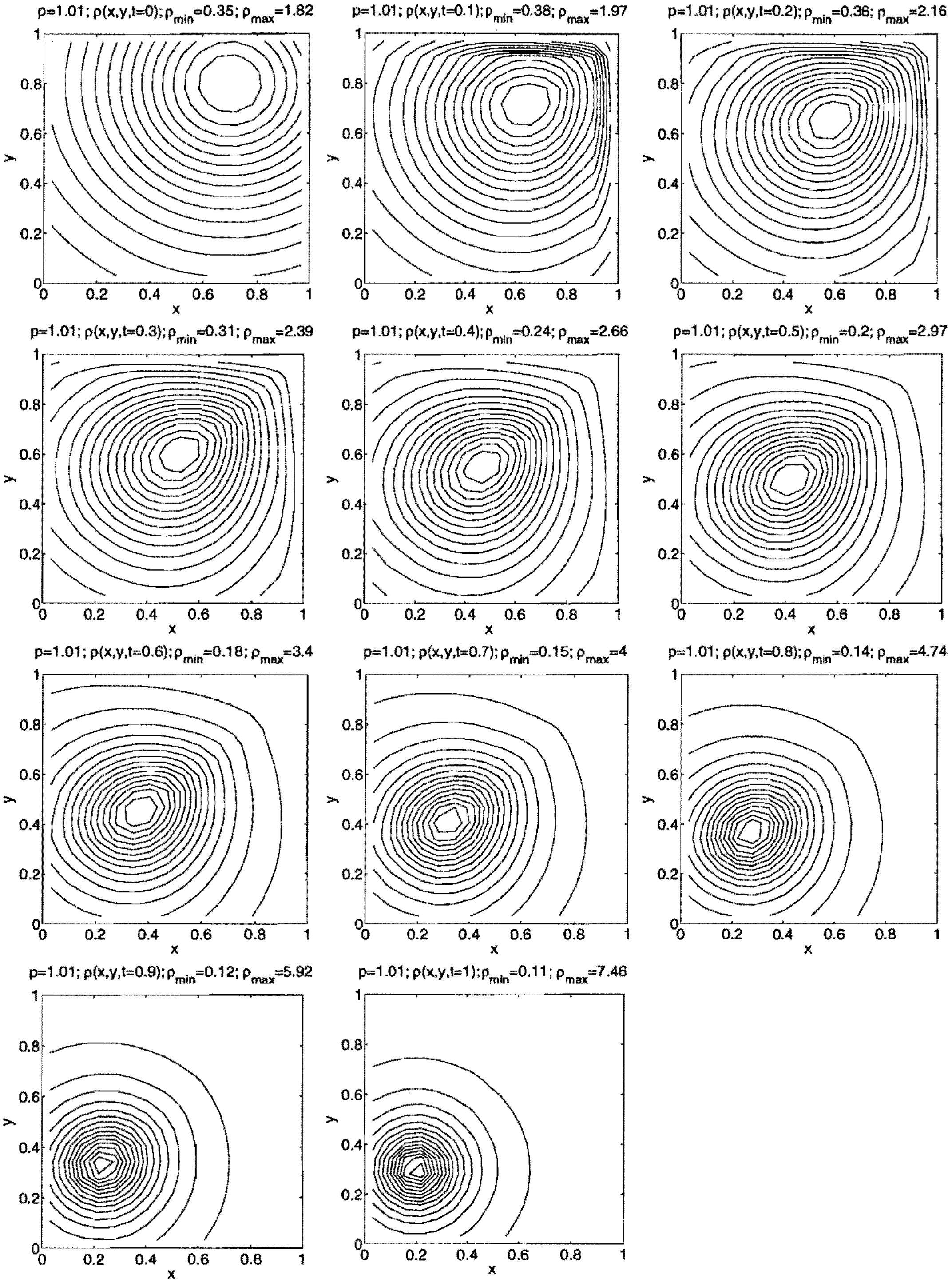

Fig. 3. Contours of the density evolution from the fluid dynamic formulation with $p = 1.01$ for the densities given by Eqs. (58). Each subplot shows 15 equally spaced density contours.

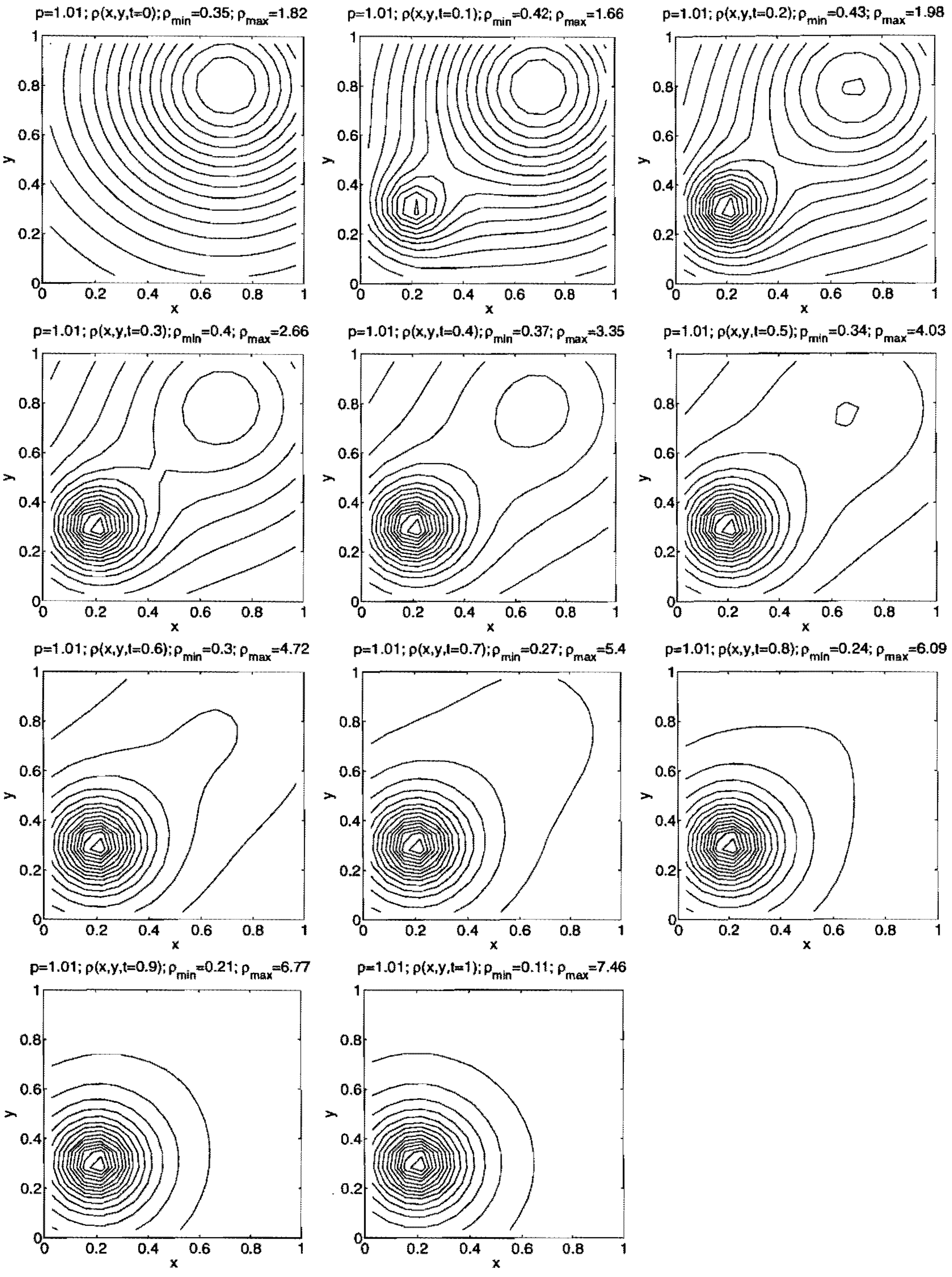

Fig. 4. Contours of the density evolution according to Eq. (40) for the densities given by Eqs. (58), with each subplot showings 15 equally spaced density contours.

6.3 Comparison of the fluid dynamic formulation with the optimal deformation method

In this subsection, we compare the fluid dynamic formulation with the optimal deformation method. As discussed in Sec. 4, the optimal deformation is defined in the limit $p \longrightarrow 1$, for which the method is linked to the L_1 MK variational principle. However, we perform the comparison also for $p > 1$, where the method is not actually related to a variational principle. The results are shown in Fig. 5 for the same densities given by Eq. (58). The solid lines are the grid lines obtained with the optimal deformation method of Sec. 4 [Eqs. (47) and (48)], and the dashed line is from the fluid dynamic formulation of Sec. 3. In this figure, we have 32×32 cells and $p = 2, 1.5, 1.3, 1.1, 1.05, 1.01$. For large p, one can see that the two grids are completely different. We note that for $p = 2$ the optimal deformation method corresponds to the method used in Refs. [?]LJL98,germans), cf. 39. However, as $p \longrightarrow 1$ the two grids converge to the same solution. This is the numerical confirmation of the mathematical proof given by Evans and Gangbo [26] that, in the limit $p \longrightarrow 1$, the optimal deformation method is equivalent to the L_1 MK variational principle.

In Fig. 6 we show orbits obtained from the optimal deformation method. On the left we have $p = 2$ while on the right we have $p = 1.01$. The initial grid points are uniformly distributed and each trajectory shown consists of 101 points equally spaced in time. One can see that for $p = 2$ the trajectories are not straight lines. This is not surprising since for $p = 2$ the optimal deformation method does not have any link with a L_p MK variational principle (for which we have shown in Sec. 3 that grid point trajectories follow straight lines). On the other hand, for $p = 1.01$ the grid points follow straight line orbits. However, one can see from Fig. 6 that these points do not move with a constant velocity (as they do in the fluid dynamic formulation). Considering for instance the trajectory of the point starting at $x = y = 0.75$, one can see that at the beginning of the time evolution ($t \approx 0$) successive points are closely packed, then the distance between to consecutive points increases ($t \approx 0.5$), and toward the end ($t \approx 1$) consecutive points are again more closely spaced. This means that the grid point originating at $x = y = 0.75$ accelerates at the beginning and then decelerates. This is another indication that the flow in the optimal deformation method is not optimal (according to the L_p MK variational principle) and, consequently, the 'optimal' evolution of the density is not a linear interpolation between ρ_0 and ρ_1.

We conclude that for $p > 1$ the optimal deformation method bears no resemblance to the L_p map or its L_p fluid dynamical formulation, which has constant velocity orbits and densities evolving as in Figs. 2 and 3. Close to $p = 1$, on the other hand, the optimal deformation method does appear to lead to the optimal L_1 map, but the densities are very completely different

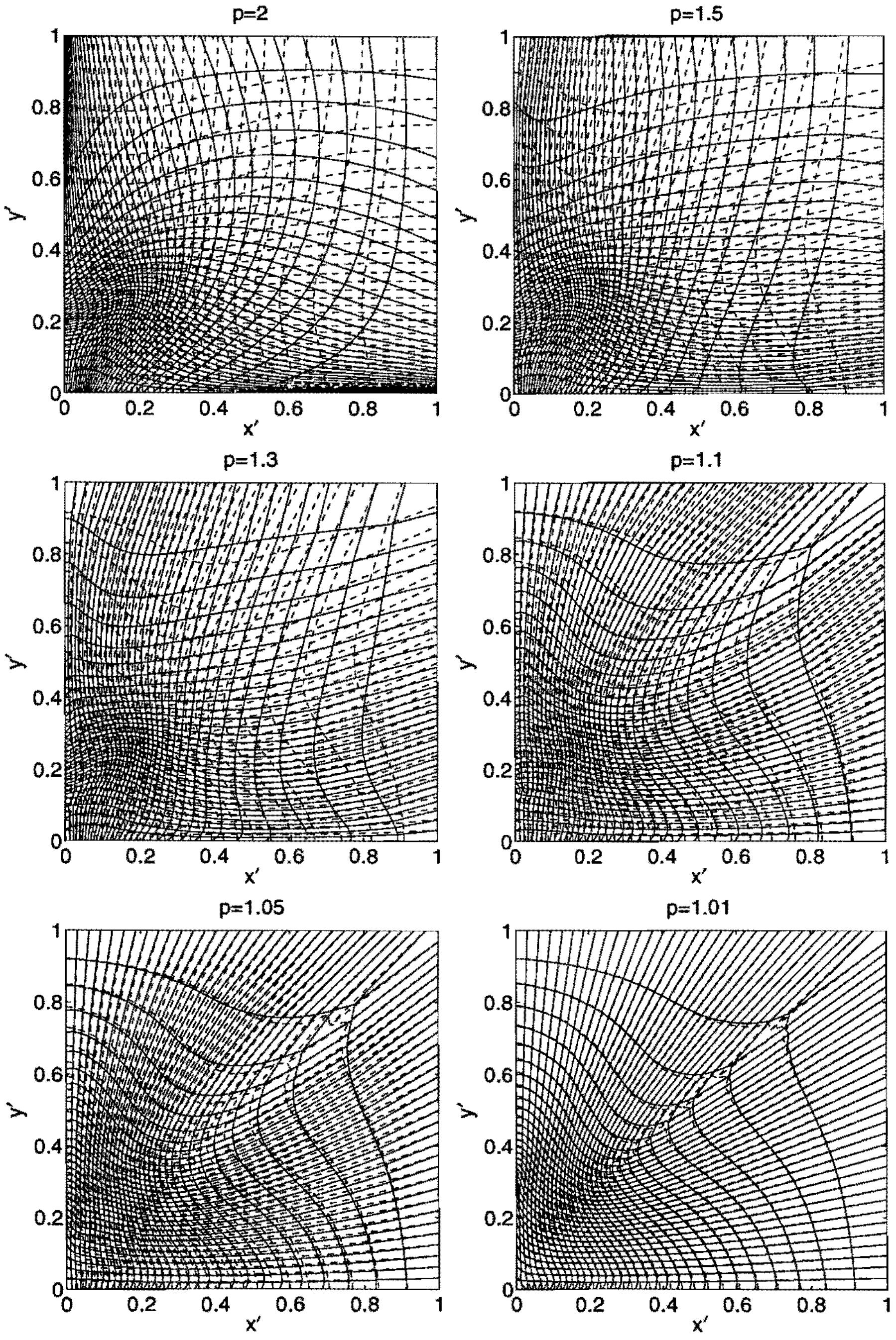

Fig. 5. Contours $x(x', y') = \text{const}$ and $y(x', y') = \text{const}$ for the optimal deformation method (solid line), which is actually optimal only for $p = 1$, and the L_p fluid dynamic formulation (dashed line) with $p = 2, 1.5, 1.3, 1.1, 1.05, 1.01$ $(32 \times 32$ cells).

and the orbits, while apparently straight lines for p close to unity, do not have constant velocity.

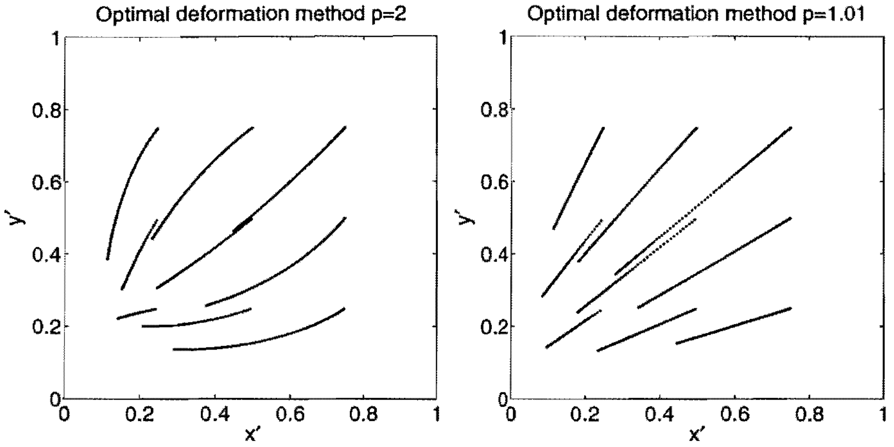

Fig. 6. Time evolution of 9 uniformly spaced grid points according to the optimal deformation method with $p = 2$ (left) and $p = 1.01$ (right). Each trajectory consists of 101 dots equally spaced in time.

6.4 *Application of the L_p fluid dynamic formulation to imaging*

In this subsection, we discuss the application of the L_p fluid dynamic formulation to find the warping transformation between two given images. In this context, the luminosity of the two images corresponds to the densities ρ_0 and ρ_1. This is motivated by recent work presented in Refs. [30–33], where L_2 MK optimization was proposed as a tool to perform the warping between two images. Zhu *et al* [32] found that L_2 MK optimization can lead to the effect of double-exposure, i. e. the fact that features of the initial image persist during the warping transformation. An example of double-exposure is the linearly interpolated density of Fig. 4. Zhu *et al.* [32] also speculated that L_p MK optimization (with $1 < p < 2$) could improve upon L_2 in terms of reducing double-exposure. Here, we wish to compare L_2 with general L_p.

Figures 2 and 3 already offer some insight. As already noted, these figures involve an initial peaked density which is advected and compressed in time, resulting in the more peaked final density ρ_1 peaked at a new position. By comparing Figs. 2 and 3, i.e. its velocity is not constant along the trajectory, it is clear that $p = 2$ performs better than $p \to 1$. This is due to the problems arising near the boundaries. Notice that Figs. 2 and 3 show no evidence of double-exposure; this is probably because the specific example is rather simple for imaging applications.

Further insight can be gained by considering also the following example

$$\rho_0(\mathbf{x}_0) = C_3 \exp\left[-2(x_0 - 0.5)^2 - 10(y_0 - 0.5)^2\right]$$

$$\rho_1(\mathbf{x}_1) = C_4 \exp\left[-10(x_1-0.5)^2 - 2(y_1-0.5)^2\right] \tag{59}$$

where again C_3 and C_4 are normalization constants. This example corresponds to an initial peaked density which is rotated by 90 degrees to give the final density. The time evolution of the density is shown in Fig. 7 for $p = 2$ and in Fig. 8 for $p = 1.01$. For $p = 2$, one can see that the density is compressed in the x direction and expands in the y direction. (Notice that at $t = 0.5$ the density appears to be approximately rotationally symmetric.) This evolution does not correspond to a pure rotation, which would be the simplest warping transformation between ρ_0 and ρ_1. The fact that L_2 MK optimization cannot capture a pure rotation is not surprising, since for $p = 2$ the flow is a gradient flow and therefore curl-free. The evolution for $p = 1.01$ is very similar to that of $p = 2$. As in Fig. 3, the interaction with the boundary creates problems. In this specific example, it generates artificial structures near the midpoints of the boundary segments. Again, the evolution for $p = 1.01$ does not correspond to a rotation. This has some significance since in principle the flow is not a gradient flow for $p = 1.01$.

We conclude based on these few examples that $p = 2$ performs better than $p \to 1$ for image warping applications, primarily because of issues related to the boundary for small p. We have noted that $p = 2$ does a reasonable job for an example where the feature of the initial image is primarily moved to a different location (Fig. 2), but it cannot move an initial image to a rotated form of the image via a flow involving rotation, because for $p = 2$ both the map and the flow are gradients.

7 Conclusions

In this paper we have analyzed some of the equidistribution methods described in the literature and their application to grid generation. These are methods where the Jacobian of the map satisfies a prescribed distribution $\det\nabla\mathbf{x}_1(\mathbf{x}_0) = \rho_0(\mathbf{x}_0)/\rho_1(\mathbf{x}_1)$. There are essentially two kinds of equidistribution methods in the literature. The first kind consists of a minimization procedure where the equidistribution principle is enforced locally by a Lagrange multiplier [8,9,11]. In this class, we have focused on the so-called L_p Monge-Kantorovich optimization [8,9,11], where the L_p norm of $\mathbf{x}_1 - \mathbf{x}_0$ is minimized. The second kind is the deformation method [12], where the equidistribution principle is satisfied by a continuous deformation in time of the initial condition. In the deformation method there is a degree of freedom in choosing the flow responsible for the deformation procedure.

While this work complements and extends previous work on these equidistri-

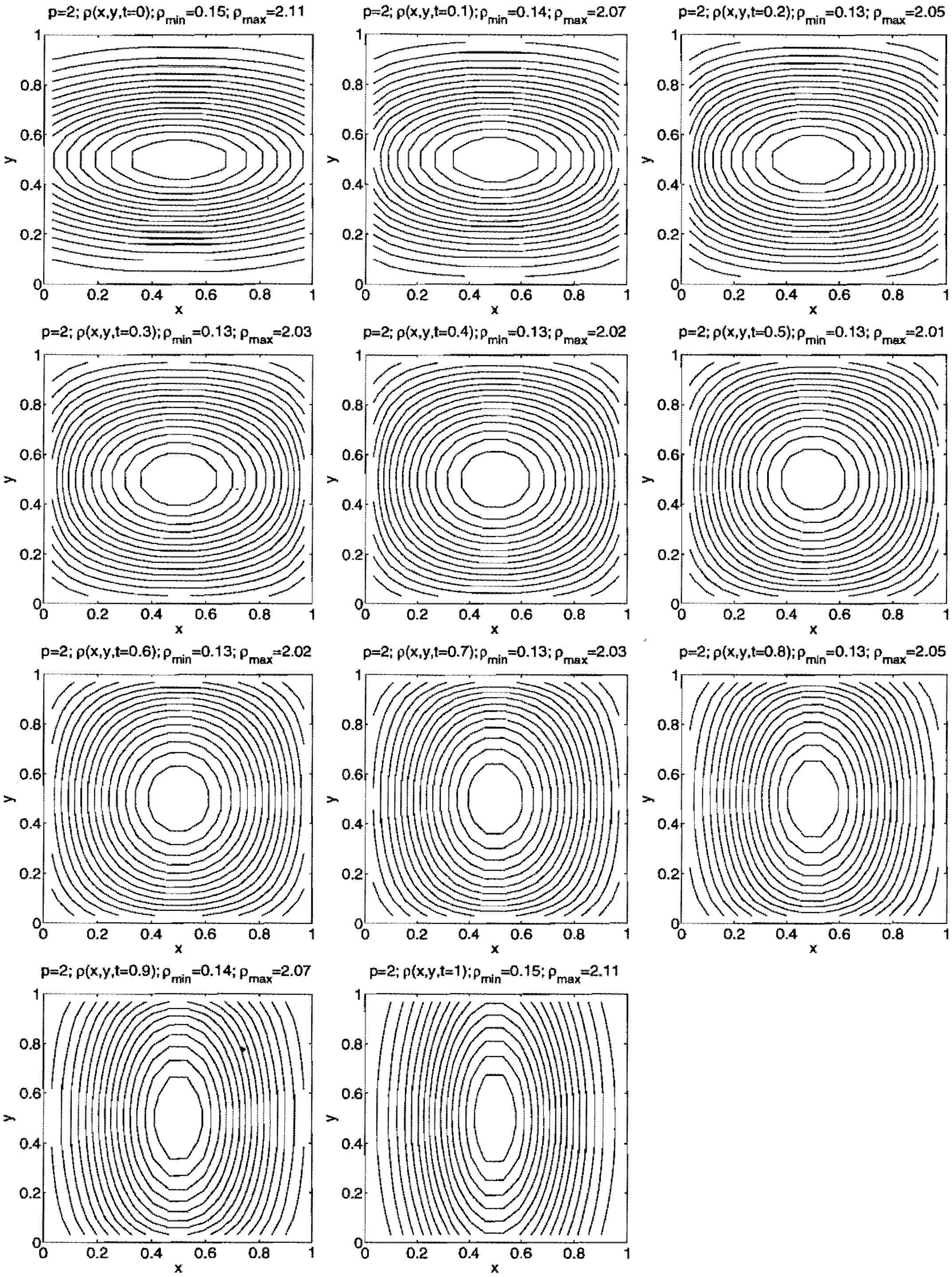

p=2; ρ(x,y,t=0); ρ_{min}=0.15; ρ_{max}=2.11

p=2; ρ(x,y,t=0.1); ρ_{min}=0.14; ρ_{max}=2.07

p=2; ρ(x,y,t=0.2); ρ_{min}=0.13; ρ_{max}=2.05

p=2; ρ(x,y,t=0.3); ρ_{min}=0.13; ρ_{max}=2.03

p=2; ρ(x,y,t=0.4); ρ_{min}=0.13; ρ_{max}=2.02

p=2; ρ(x,y,t=0.5); ρ_{min}=0.13; ρ_{max}=2.01

p=2; ρ(x,y,t=0.6); ρ_{min}=0.13; ρ_{max}=2.02

p=2; ρ(x,y,t=0.7); ρ_{min}=0.13; ρ_{max}=2.03

p=2; ρ(x,y,t=0.8); ρ_{min}=0.13; ρ_{max}=2.05

p=2; ρ(x,y,t=0.9); ρ_{min}=0.14; ρ_{max}=2.07

p=2; ρ(x,y,t=1); ρ_{min}=0.15; ρ_{max}=2.11

Fig. 7. Contours of the density evolution from the fluid dynamic formulation with $p = 2$ for the densities given by the linear interpolation formula of Eqs. (59). Each subplot shows 15 equally spaced contours of the density.

$p=1.01$; $\rho(x,y,t=0)$; $\rho_{min}=0.15$; $\rho_{max}=2.11$

$p=1.01$; $\rho(x,y,t=0.1)$; $\rho_{min}=0.15$; $\rho_{max}=2.11$

$p=1.01$; $\rho(x,y,t=0.2)$; $\rho_{min}=0.15$; $\rho_{max}=2.11$

$p=1.01$; $\rho(x,y,t=0.3)$; $\rho_{min}=0.15$; $\rho_{max}=2.11$

$p=1.01$; $\rho(x,y,t=0.4)$; $\rho_{min}=0.15$; $\rho_{max}=2.11$

$p=1.01$; $\rho(x,y,t=0.5)$; $\rho_{min}=0.15$; $\rho_{max}=2.11$

$p=1.01$; $\rho(x,y,t=0.6)$; $\rho_{min}=0.15$; $\rho_{max}=2.11$

$p=1.01$; $\rho(x,y,t=0.7)$; $\rho_{min}=0.15$; $\rho_{max}=2.11$

$p=1.01$; $\rho(x,y,t=0.8)$; $\rho_{min}=0.15$; $\rho_{max}=2.11$

$p=1.01$; $\rho(x,y,t=0.9)$; $\rho_{min}=0.15$; $\rho_{max}=2.11$

$p=1.01$; $\rho(x,y,t=1)$; $\rho_{min}=0.15$; $\rho_{max}=2.11$

Fig. 8. Contours of the density evolution from the fluid dynamic formulation with $p = 1.01$ for the densities given by Eqs. (59). Each subplot shows 15 equally spaced density contours.

bution methods, there are four main contributions:

(1) We have shown that L_p MK optimization and the related generalized L_p MA equation are equivalent to a L_p fluid dynamic formulation in which a density obeying a continuity equation is advected by an optimal time-dependent flow for $0 \leq t \leq 1$. Therefore we present an alternative, fluid dynamic method to reach the same equidistributed grid. While the solution of the generalized L_p MA equation (for which multigrid preconditioning can work effectively) is our preferred way of computing the new grid, this alternative method could be used if the other one fails. In this regard, further work will be needed to find a suitable preconditioner for the fluid dynamic method.

(2) We have shown that the deformation method belongs to the family of fluid methods. Thus this paper provides a unified theory of the equidistribution methods based on L_p MK optimization and the deformation method. The deformation method is obtained from a fluid formulation by assuming that the density evolves according to a linear interpolation in time between the initial and final densities ρ_1 and ρ_2, and the velocity obeys the continuity equation using this density. There is nothing special about the linear interpolation assumption and one could generate an infinite number of alternative deformation methods by simply assuming more complicated time dependences of the density. However, the linear interpolation in time is convenient from a practical point of view since it gives rise to the simplest deformation method. Notice that, in general, when an assumption is made on the time evolution of the density in the fluid dynamic formulation (but without any assumption on the form of the flow), any link with the underlying variational principle is lost.

(3) Following the work by Evans and Gangbo [26], we have shown that the deformation method can be linked to L_1 MK optimization by a suitable choice of the flow. This aspect has not been recognized in the literature related to the deformation method and, while theoretically developed by Evans and Gangbo [26] (not in the context of grid generation but as a proof of the existence of a solution of the L_1 MK problem), it has been verified with numerical experiments here for the first time.

(4) We have explored the application of the L_p fluid dynamic formulation developed here to imaging techniques. Specifically, the fluid dynamic formulation in which a density is advected from an initial to a final density is equivalent to a warping transformation between the two images. Here the luminosity of the two images corresponds to the initial and final densities. L_2 MK optimization was applied to image warping in Refs. [30–32], where it was argued that future work might focus on L_p with $1 < p < 2$, which could offer improvements over $p = 2$. We have checked this hypothesis and concluded that the L_2 method is better than the L_p method for $p < 2$ because for smaller p artificial structures arise near the boundary. (This type of problem has also been documented for the L_p map problem

in Ref. [11].) However, based on our results it is far from clear that the $p = 2$ fluid dynamic formulation provides a competitive method for image warping.

Acknowledgements

This research was performed under the auspices of the National Nuclear Security Administration of the U.S. Department of Energy at Los Alamos National Laboratory (LANL), operated by LANS LLC under contract DE-AC52-06NA25396. It was supported by the Laboratory Directed Research and Development program at LANL. The authors acknowledge enlightening discussions with Luis Chacón, Rick Chartrand, L. Craig Evans, Wilfrid Gangbo and Patrick Knupp.

Appendix A. Fluid momentum equation for L_p

In this appendix we show details of the derivation of Eq. (26). Using Eq. (12) leads to

$$\begin{aligned}\partial_t \mathbf{v} &= \frac{2-p}{p-1}|\nabla S|^{\frac{4-3p}{p-1}}\nabla S\nabla S\cdot\partial_t S + |\nabla S|^{\frac{2-p}{p-1}}\nabla\partial_t S \\ &= f^{\frac{2-p}{p-1}}\left(\frac{2-p}{p-1}\hat{\mathbf{e}}\hat{\mathbf{e}}\cdot\nabla\partial_t S + \nabla\partial_t S\right),\end{aligned} \tag{60}$$

where $f = |\nabla S|$ and $\hat{\mathbf{e}} = \nabla S/|\nabla S|$. Equation (23) implies $\nabla\partial_t S = -f^{\frac{1}{p-1}}\nabla S$. Substituting into Eq. (60), we obtain

$$\partial_t \mathbf{v} = -f^{\frac{3-p}{p-1}}\left(\nabla f + \frac{2-p}{p-1}\hat{\mathbf{e}}\hat{\mathbf{e}}\cdot\nabla f\right). \tag{61}$$

Once more using Eq. (12) we find

$$\nabla\times\mathbf{v} = \frac{2-p}{p-1}f^{\frac{3-2p}{p-1}}\nabla f\times\nabla S \quad \text{and} \tag{62}$$

$$\begin{aligned}\mathbf{v}\times\nabla\times\mathbf{v} &= f^{\frac{5-3p}{p-1}}\frac{2-p}{p-1}\nabla S\times(\nabla f\times\nabla S) \\ &= f^{\frac{3-p}{p-1}}\frac{2-p}{p-1}\left(\nabla f - \hat{\mathbf{e}}\hat{\mathbf{e}}\cdot\nabla f\right).\end{aligned} \tag{63}$$

Using Eq. (12) again, we find

$$\nabla \frac{\mathbf{v}^2}{2} = \frac{1}{p-1} f^{\frac{3-p}{p-1}} \nabla f. \tag{64}$$

Putting all this together, we find $\partial_t \mathbf{v} - \mathbf{v} \times \nabla \times \mathbf{v} + \nabla \mathbf{v}^2/2 = 0$, that is

$$\partial_t \mathbf{v} + \mathbf{v} \cdot \nabla \mathbf{v} = 0, \tag{65}$$

implying constant velocity trajectories.

References

[1] J. F. Thompson, "Survey of dynamically-adaptive grids in the numerical solution of partial differential equations," *Applied Numerical Mathematics*, vol. 1, no. 1, pp. 3 – 27, 1985.

[2] P. R. Eiseman, "Adaptive grid generation," *Computer Methods in Applied Mechanics and Engineering*, vol. 64, no. 1-3, pp. 321 – 76, 1987.

[3] D. A. Anderson, "Equidistribution schemes, Poisson generators, and adaptive grids," *Applied Mathematics and Computation*, vol. 24, no. 3, pp. 211 – 227, 1987.

[4] W. Huang, Y. Ren, and R. D. Russell, "Moving mesh partial differential equations (MMPDES) based on the equidistribution principle," *SIAM J. Numer. Anal.*, vol. 31, no. 3, pp. 709–730, 1994.

[5] M. J. Baines, "Least squares and approximate equidistribution in multidimensions," *Numerical Methods for Partial Differential Equations*, vol. 15, no. 5, pp. 605 – 615, 1999.

[6] G. Lapenta, "Variational grid adaptation based on the minimization of local truncation error: Time independent problems," *J. Comput. Phys.*, vol. 193, p. 159, 2004.

[7] J. U. Brackbill and J. S. Saltzman, "Adaptive zoning for singular problems in 2 dimensions," *J. Comput. Phys.*, vol. 46, no. 3, pp. 342–368, 1982.

[8] G. L. Delzanno, L. Chacón, J. M. Finn, Y. Chung, and G. Lapenta, "An optimal robust equidistribution method for two-dimensional grid adaptation based on Monge-Kantorovich optimization," *J. Comput. Phys.*, vol. 227, no. 23, pp. 9841–9864, 2008.

[9] J. M. Finn, G. L. Delzanno, and L. Chacón, "Grid generation and adaptation by Monge-Kantorovich optimization in two and three dimensions," *Proceedings of the 17th International Meshing Roundtable, Pittsburgh, PA, USA*, p. 551, 2008.

[10] C. J. Budd and J. F. Williams, "Moving mesh generation using the parabolic Monge-Ampère equation," *SISC, submitted*, vol. xx, p. xxxx, 2009.

[11] G. L. Delzanno and J. M. Finn, "Generalized Monge-Kantorovich optimization for grid generation and adaptation in l_p," *SISC, submitted*, 2009.

[12] G. Liao and D. Anderson, "A new approach to grid generation," *Appl. Anal.*, vol. 44, pp. 285–297, 1992.

[13] J. Moser, "On volume elements on a manifold," *Transactions of the American Mathematical Society*, vol. 120, no. 2, pp. 286 – 294, 1965.

[14] B. Dacorogna and J. Moser, "On a partial-differential equation involving the jacobian determinant," *Annales de l'Institut Henri Poincaré. Analyse non Linéaire*, vol. 7, no. 1, pp. 1 – 26, 1990.

[15] G. Liao and J. Su, "Grid generation via deformation," *Applied Mathematics Letters*, vol. 5, no. 3, pp. 27–29, 1992.

[16] J. D. Benamou and Y. Brenier, "Mixed L2-wasserstein optimal mapping between prescribed density functions," *J. Optimization Theory Appl.*, vol. 111, p. 255, 2001.

[17] J. D. Benamou, Y. Brenier, and K. Guillet, "The Monge-Kantorovich mass transfer and its computational fluid dynamics formulation," *International J. Num. Methods in Fluids*, vol. 40, p. 21, 2002.

[18] P. Morrison, *Encyclopedia of Mathematical Physics*, ch. Hamiltonian Fluid Dynamics. Elsevier, to appear, 2009.

[19] A. Banyaga, "Formes volume sur es varietes a bord," *Enseignement Math.*, vol. 20, pp. 127 – 131, 1974.

[20] G. Liao, T. Pan, and J. Su, "Numerical grid generator based on Moser's deformation method," *Numerical Methods for Partial Differential Equations*, vol. 10, no. 1, pp. 21–31, 1994.

[21] F. Liu, S. H. Ji, and G. J. Liao, "Adaptive grid method and its application to steady Euler flow calculations," *SIAM Journal on Scientific Computing*, vol. 20, no. 3, pp. 811 – 825, 1998.

[22] B. Semper and G. Liao, "A moving grid finite-element method using grid deformation," *Numerical Method for PDEs*, vol. 11, pp. 603 – 615, 1995.

[23] P. Bochev, G. Liao, and G. D. Pena, "Analysis and computation of adaptive moving grids by deformation," *Numerical Method for PDEs*, vol. 12, pp. 489 – 506, 1996.

[24] M. Cho and S. Jun, "r-adaptive mesh generation for shell finite element analysis," *J. Comput. Phys.*, vol. 199, no. 1, pp. 291 – 316, 2004.

[25] M. Grajewski, M. Koster, and S. Ture, "Mathematical and numerical analysis of a robust and efficient grid deformation method in the finite element context," *SIAM J. Sci. Comput.*, vol. 31, no. 2, pp. 1539–1557, 2009.

[26] L. C. Evans and W. Gangbo, "Differential equations methods for the Monge-Kantorovich mass transfer problem," *Memoirs of the American Mathematical Society*, vol. 137, no. 653, p. 1, 1999.

[27] N. Trudinger and X. Wang, "On the Monge mass transfer problem," *Calculus of Variations and Partial Differential Equations*, vol. 13, no. 1, pp. 19–31, 2001.

[28] L. Caffarelli, M. Feldman, and R. McCann, "Constructing optimal maps for Monge transport problem as a limit of strictly convex costs," *Journal of the American Mathematical Society*, vol. 15, no. 1, pp. 1–26, 2002.

[29] C. T. Kelley, *Iterative Methods for Linear and Nonlinear Equations.* SIAM, Philadelphia, 1995.

[30] S. Angenent, S. Haker, and A. Tannenbaum, "Minimizing flows for the Monge-Kantorovich problem," *SIAM Journal on Mathematical Analysis*, vol. 35, no. 1, pp. 61–97, 2003.

[31] S. Haker, L. Zhu, A. Tannenbaum, and S. Angenent, "Optimal mass transport for registration and warping," *International Journal of Computer Vision*, vol. 60, no. 3, pp. 225–40, 2004.

[32] L. Zhu, Y. Yang, S. Haker, and A. Tannenbaum, "An image morphing technique based on optimal mass preserving mapping," *IEEE Transactions on Image Processing*, vol. 16, no. 6, pp. 1481–95, 2007.

[33] R. Chartrand, K. Vixie, B. Wohlberg, and E. Bollt, "A gradient descent solution to the Monge-Kantorovich problem," *A visualization journal, to appear*, vol. xx, p. xxxx, 2009.